Check for updates

Influence of collector doping setback in the quantum transport characteristics of GaN/AlN resonant tunneling diodes

Jimy Encomendero[1]* , Vladimir Protasenko[1], Debdeep Jena[1,2,3], and Huili Grace Xing[1,2,3]*

[1]School of Electrical and Computer Engineering, Cornell University, Ithaca, New York 14853, United States of America
[2]Department of Materials Science and Engineering, Cornell University, Ithaca New York 14853, United States of America
[3]Kavli Institute at Cornell for Nanoscale Science, Ithaca, New York 14853, United States of America

*E-mail: jje64@cornell.edu; grace.xing@cornell.edu

Harnessing resonant tunneling transport in III-nitride semiconductors to boost the operating frequencies of electronic and photonic devices, requires a thorough understanding of the mechanisms that limit coherent tunneling injection. Towards this goal, we present a concerted experimental and theoretical study that elucidates the impact of the collector doping setback on the quantum transport characteristics of GaN/AlN resonant tunneling diodes (RTDs). Employing our analytical model for polar RTDs, we quantify the width of the resonant-tunneling line shape, demonstrating that the setback helps preserve coherent injection. This design results in consistently higher peak-to-valley-current ratios (PVCRs), obtaining a maximum PVCR = 2.01 at cryogenic temperatures. © 2021 The Japan Society of Applied Physics

Resonant tunneling transport holds promise for the development of high-power terahertz sources required in a plethora of applications spanning from high-speed broadband communication networks,[1–4] to medical imaging,[5] and chemical detectors.[6] The technological importance of this quantum transport regime stems from the possibility of engineering the underlying carrier transport dynamics by means of heterostructure design.[7,8] This approach enables control over the injection and depopulation times of quantum-confined electronic subbands, thereby attaining ultra-fast carrier transport for high-speed oscillators,[9–11] and population inversion for high-power intersubband lasers.[12]

Over the last few years, resonant tunneling within III-nitride semiconductors has undergone a renaissance, thanks to recent breakthroughs in epitaxial growth, heterostructure design, and device fabrication techniques.[13–24] Since the first demonstration of repeatable room temperature negative differential conductance (NDC) in GaN/AlN resonant tunneling diodes (RTDs),[14,15] there has been a steady improvement in the current densities delivered by these devices.[23,24] More importantly, the robustness of this quantum transport regime has been experimentally verified with the demonstration of the first resonant tunneling microwave oscillator.[24,25] These milestones highlight the exciting prospects of nitride-based resonant tunneling injection for the engineering of new functionalities within the family of III-nitride electronic and photonic devices.[26–29]

In contrast to traditional non-polar semiconductors, III-nitride heterostructures exhibit strong built-in polarization fields which dominate their electronic, optical, and piezoelectric properties. Owing to their magnitude, they influence the distribution of free carriers, control the strength and direction of the internal electric fields, and determine the conduction-band profile of the resonant tunneling cavity. These important effects can be seen in Fig. 1, which shows two different GaN/AlN double-barrier heterotructure designs studied in this report. As can be seen from Fig. 1(d), the heterojunction between the AlN barrier and GaN contact, on the collector side, hosts a negative polarization charge $-q\sigma_\pi$, which repels free carriers and induces a depletion region. This polarization-induced effect not only widens the effective collector tunneling distance, but also extends the collector

space-charge region, uncovering a high density of ionized donors right next to the resonant tunneling double-barrier structure [see Fig. 1(c)]. The consequences of this effect—unique in polar heretostructures—have not been reported in the literature. Therefore, the purpose of this report is to fill this gap, unveiling the impact of the collector design on the resonant tunneling transport characteristics of polar III-nitride RTDs.

In this paper, we present a concerted experimental and theoretical study that clarifies the role played by the collector design on the electrostatics of the polar resonant tunneling cavity. These effects are experimentally investigated by measuring the electronic transport characteristics of GaN/AlN RTDs with different collector doping setbacks. Employing our analytical quantum transport model for polar RTDs, we quantify the broadening of the resonant tunneling line shape, conclusively demonstrating that the inclusion of the doping setback helps preserve coherent injection. This improved RTD design allows us to measure consistently higher peak-to-valley current ratios (PVCRs), obtaining a high PVCR of 2.01 at cryogenic temperatures.

To experimentally determine the consequences of the polarization-induced depletion region on the quantum transport characteristics, we prepare two RTD structures with different collector designs [see Figs. 1(a) and 1(b)]. Molecular beam epitaxy is employed to synthesize the heterostructures, maintaining precise control over the layer thicknesses, and preserving step-flow growth mode under metal-rich conditions. Throughout the whole epitaxial process, we monitor the oscillating intensity of the reflection high-energy electron diffraction pattern to measure—in real time—the incorporation of single monolayers.[22,30] These conditions, allow us to maintain the high structural quality of the single-crystal n-GaN substrates, minimizing the presence of crystalline defects and threading dislocations.

Epitaxy begins with the growth of the n-type GaN emitter contact, doped with a concentration of silicon donors: $N_d \approx 1 \times 10^{19}$ cm^{-3}. The active region consists of a 10 nm thick unintentionally-doped (UID) GaN spacer that separates the highly-doped n-GaN emitter layer from the AlN/GaN/AlN (2/3/2 nm) resonant tunneling cavity. The double-barrier heterostructure is grown following the epitaxial procedure detailed in Ref. 22 allowing us to deterministically control
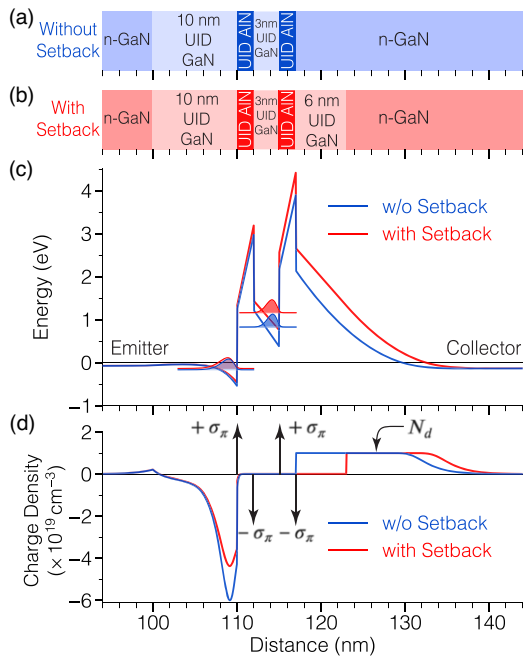
Fig. 1. (Color online) Schematic cross-section of the GaN/AlN RTDs studied in this report. Both devices have the same double-barrier resonant tunneling cavity, but different collector designs. Panel (a) shows the RTD design devoid of any doping setback between the collector AlN-barrier and the n-type GaN contact layer. Panel (b) displays the RTD structure incorporating a 6 nm thick collector doping setback. (c) A self-consistent Schrödinger–Poisson solver is used to calculate the conduction-band diagrams at equilibrium. The charge density profile of both structures is shown in panel (d).

the barrier thickness and well width of our devices. Two different designs were prepared: sample (a) devoid of any doping setback between the collector AlN-barrier and the n-type GaN layer; and sample (b) featuring a 6 nm UID-GaN collector doping setback [see Figs. 1(a) and 1(b)]. The extension of the collector setback is solely determined by the growth rate, which is kept constant at $\sim 3 \, \mathrm{nm \, min^{-1}}$ throughout the whole epitaxial process, without the inclusion of any growth interruption. Both structures were terminated with a 100 nm thick n-type GaN collector electrode. After epitaxy, both samples were characterized by X-ray diffraction, revealing clear Pendellösung interference fringes, attesting to the high quality of the heterointerfaces.[31] Atomic force microscopy is also employed to scan the surface of the samples, revealing a topography characterized by atomic steps and sub-nanometer root-mean-square roughness. Finally, RTDs are fabricated using a conventional fabrication procedure, described in a previous report.[19]

Electronic transport is measured initially at room temperature under both bias polarities. Forward current injection corresponds to the electronic flow from the substrate to the collector contact, as shown schematically in the inset of Fig. 2(b). Within this transport regime, an NDC region is observed in each RTD structure, corresponding to the onset of resonant injection into the ground state of the well. This behavior is highly reproducible across multiple samples and has been measured in a large set of devices exhibiting different mesa areas varying between 36 and 400 $\mu \mathrm{m}^2$. The repeatable resonant tunneling transport is confirmed by performing double-sweep scans over both bias polarities

with injection currents up to 10 kA/cm^2. Figures 2(a) and 2(b) display the current–voltage (J–V) characteristics measured at room temperature, from diodes with mesa areas of $\approx 36 \, \mu \mathrm{m}^2$. The introduction of the collector doping setback results in a clear shift in the resonant tunneling voltage. The root cause of this effect is the intense electric field across the 6 nm thick doping setback, whose magnitude has been numerically calculated to be $\approx 5 \, \mathrm{MV \, cm^{-1}}$ at resonance. Therefore, we expect to measure a resonant tunneling voltage shift of approximately $\Delta V_{\mathrm{RES}} \approx 6 \, \mathrm{nm} \times 5 \, \mathrm{MV \, cm^{-1}} = 3 \, \mathrm{V}$, which is in good quantitative agreement with our experiments: $\Delta V_{\mathrm{RES}} = 3.2 \, \mathrm{V}$. From Fig. 1(c), we can see that the inclusion of the collector spacer not only modifies the electric field profile, but also increases the tunneling distance across the collector barrier. Consequently, due to the exponential relationship between the tunneling path and the electronic transmission, a lower current density is expected from the structure that includes the doping setback. This exponential attenuation in the tunneling current is experimentally corroborated over both bias polarities, as can be seen from the semilogarithmic plot of Fig. 2(b).

The combined experimental and theoretical analysis presented above, enables us to understand the role played by the collector design on the resonant voltage and magnitude of the peak tunneling current. These effects were initially studied in arsenide-based RTDs, employing both theoretical analysis as well as systematic experimental measurements.[32–35] Pioneering reports revealed that the collector setback not only modifies the RTD electrostatics, but also impacts the phase coherence of the electrons traversing the resonant tunneling structure. Muto et al. found that both the PVCR as well as the peak voltage of AlGaAs/GaAs RTDs increase as the extent of doping setback is varied between 0 and 15 nm.[34] A decade later, Oobo et al. published a combined experimental and theoretical study, concluding that the width of the resonant level decreases with increasing setback thickness.[35]

In this report, we study the important effects of the collector design on the phase coherence of the injected electrons, at cryogenic temperatures, using liquid nitrogen. At 77 K, the longer electronic coherence lengths enable the measurement of an additional inflection in the low-temperature J–V characteristics as indicated by the arrows in Figs. 2(c) and 2(d). This feature stems from resonant tunneling injection of carriers from the continuum of electronic states at the emitter Fermi sea, into the ground state of the well [see Fig. 3(a)]. In contrast to non-polar RTDs, the emitter region of polar double-barrier structures contains not only a Fermi sea due to uniform impurity doping, but also a 2D-electronic subband due to built-in polarization doping. As can be seen from Fig. 1(b), both 3D and 2D electronic states are populated and coexist at equilibrium conditions. Consequently, under forward bias, two type of resonances arise when carriers are injected into the ground state. Each of these resonant configurations is shown in the band diagrams of Figs. 3(a) and 3(b), and correspond to the injection of electrons from the continuum and 2D electron gas (2DEG), respectively. In our RTDs, we experimentally identify the presence of each of these tunneling injection regimes by analyzing their differential conductance versus voltage (G–V) characteristics.
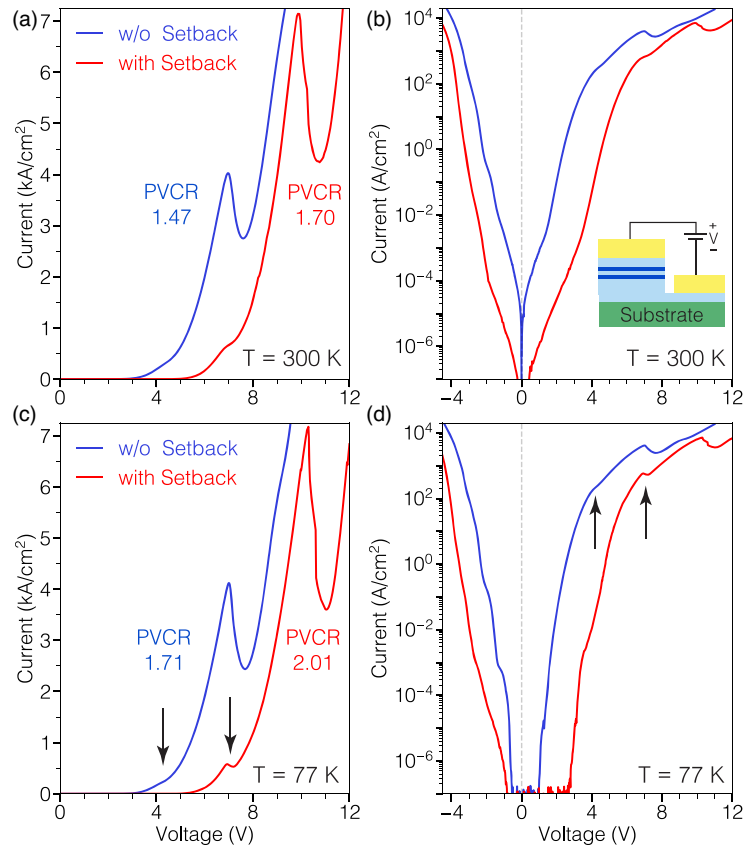
Fig. 2. (Color online) Electronic transport is measured for both RTD designs shown in Fig. 1 at room temperature and 77 K, using liquid nitrogen. (a) At room temperature, the forward current–voltage (J–V) characteristics exhibit a resonant tunneling peak with a maximum current density of 4.2 and 7.2 kA cm^{-2} for the RTD with and without the doping setback, respectively. (b) The logarithmic plot of the data displayed in panel (a), reveals the exponential modulation of the tunneling current under both bias polarities. The inset in panel (b) shows schematically the biasing circuit employed during forward bias injection. (c) The cryogenic J–V curves are measured from the same devices shown in panels (a) and (b). Panel (d) displays the logarithmic plot of the cryogenic J–V characteristics from (c). Notice the exponential modulation of the tunneling current spanning 11 orders of magnitude on both bias directions. The arrows indicate tunneling features arising due to electronic injection from emitter Fermi sea into the resonant level, as illustrated in Fig. 3(a).
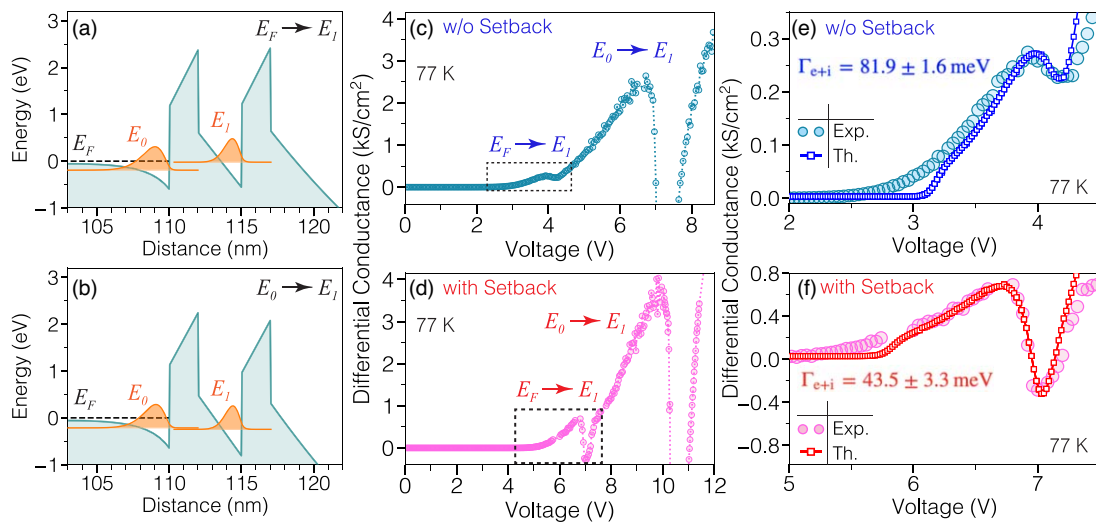

Fig. 3. (Color online) Under forward current injection, two distinct resonant tunneling configurations are attained in polar III-nitride RTDs. (a) The first resonance is due electrons tunneling from 3D scattering states in the emitter, to the resonant level E_1. (b) At slightly higher voltage bias, the 2D electron gas E_0 aligns with the ground state E_1, giving rise to the main resonant tunneling peak in the current–voltage characteristics. (c)–(d) Each of these resonances are identified in the cryogenic differential conductance of our devices, obtained by numerical differentiation of the experimental J–V characteristics displayed in Fig. 2(d). (e)–(f) Using the total width of the ground state (Γ_{e+i}) as a fitting parameter, we reproduce the experimentally measured differential conductance of both RTD structures around the first resonant tunneling peak ($E_F \rightarrow E_1$), delimited by the dashed rectangles. Panels (e) and (f) show a good quantitative agreement between the experimentally measured differential conductance (filled circles) and the theoretical calculations obtained using our quantum transport model (continuous line with empty squares). The best fit for the resonant tunneling width is shown in each figure. The error in the value of Γ_{e+i} corresponds to limits of the 95% confidence interval of the fitting procedure.

Figures 3(c) and 3(d) display the G–V curves for each RTD design, obtained by numerical differentiation of the cryogenic J–V characteristics. Both curves display two conductance maxima, labeled as $E_F \rightarrow E_1$ and $E_0 \rightarrow E_1$, and correspond to the bias conditions indicated by the energy-band diagrams of Figs. 3(a) and 3(b), respectively. The strongest conductance peak ($E_0 \rightarrow E_1$) is due to tunneling from the 2DEG into the quantum well. Within this injection regime, the momentum quantization along the transport direction gives rise to a considerable detuning from the resonant tunneling condition, enabling a robust NDC that can be measured over a wide temperature window. In contrast, the conductance peak $E_F \rightarrow E_1$, associated with the supply of carriers from 3D states within the emitter, gives rise to a weaker conductance modulation on the rising side of the main conductance peak. Interestingly, this tunneling feature exhibits different modulation strengths, depending on the extension of the collector doping setback. Figure 3(e) reveals that electronic transport across the RTD without the doping setback results in a weak modulation with a peak and valley conductance, measured at $G_{peak} = 0.28$ kS cm^{-2} and $G_{valley} = 0.22$ kS cm^{-2}, respectively. In contrast, Fig. 3(f) shows that by introducing the 6 nm thick doping setback, a stronger conductance modulation is measured, resulting in an NDC with a minimum valley conductance: $G_{valley} \approx -0.32$ kS cm^{-2}. This result indicates that placing the dopants further away from the resonant tunneling cavity enhances its quantum interference properties.

To gain further insight into the physical processes that determine quantum interference effects in polar heterostructures, we employ our analytical model for GaN/AlN RTDs.[36] This theoretical framework allows us to calculate the resonant tunneling current over the entire spectrum of quantum transport regimes: from completely coherent injection to the sequential tunneling limit. Analytical expressions for the tunneling current densities $J_{E_F \rightarrow E_1}$ and $J_{E_0 \rightarrow E_1}$, corresponding to the injection regimes depicted in Figs. 3(a) and 3(b), are written as follows:[36–39]

$$J_{E_F \rightarrow E_1} = \frac{qm^\star kT}{2\pi^2 \hbar^3} T_{max} \left(\frac{\Gamma_e}{2} \right) \ln \left[\frac{\mathcal{F}_2}{\mathcal{F}_1} \right] \left[\tan^{-1} \left(\frac{E_1}{\frac{\Gamma_{e+i}}{2}} \right) + \frac{\pi}{2} \right] \quad (1)$$

and

$$J_{E_0 \rightarrow E_1} = \frac{2qm^\star kT}{\pi^2 \hbar^3} \Delta E_0 \mathcal{T}(E_0) \ln \left[\frac{\mathcal{F}_2}{\mathcal{F}_1} \right]. \quad (2)$$

Here, $m^\star$ and q are the effective mass and charge of the electron, k is the Boltzmann constant, $\hbar$ is the reduced Planck's constant, and T is the device operating temperature. $\mathcal{F}_1$ and $\mathcal{F}_2$ are the Fermi distributions on the emitter and collector contacts, respectively. E_0 and E_1 are the subband energies of the bound states in the emitter and quantum well. The resonant tunneling transmission via the ground state E_1 is approximated by the Breit–Wigner formula:

$$\mathcal{T}(E) = T_{max} \left(\frac{\Gamma_e}{\Gamma_{e+i}} \right) \frac{(\Gamma_{e+i}/2)^2}{(E - E_1)^2 + (\Gamma_{e+i}/2)^2}, \quad (3)$$

where T_{max} is the peak transmission of the resonant tunneling line shape. Γ_e is the elastic width in the fully coherent transport limit, and Γ_{e+i} is the total elastic and inelastic width of the ground state in the presence of phase randomization

events.[36] Employing expressions (1) and (2), and treating Γ_{e+i} as a phenomenological tunable parameter, we fit the experimentally measured G–V characteristics of our devices.

To quantitatively determine the broadening effects due to ionized collector impurities, we study electronic transport at 77 K. At this temperature, electron–phonon interactions are strongly suppressed; as a result, interface roughness scattering and background and remote impurities become the dominant dephasing mechanisms. In addition, it is important to note that under non-equilibrium conditions, the increasing carrier concentration in the well partially screens the scattering potential of the ionized donors. Since our goal here is to quantify the broadening effects due to collector impurities, we restrict our analysis to first resonant tunneling peak ($E_F \rightarrow E_1$). Within this regime, the lower electronic population in the well allows us to probe the scattering effects due to collector donors with minimal screening.

Figures 3(e) and 3(f) show a good quantitative agreement between the experimental and theoretical curves around the $E_F \rightarrow E_1$ peak. It is clear from these figures. that by tuning the resonance width, we can reproduce the valley conductance of both RTD designs. Using a non-linear least-squares method, we obtain a phenomenological resonance width given by $\Gamma_{e+i} = 43.5 \pm 3.3$ meV and $\Gamma_{e+i} = 81.9 \pm 1.6$ meV for the RTD structures with and without the collector doping setback, respectively. The lower and upper bounds in the fitted resonance width correspond to limits of the 95% confidence interval of the fitting procedure. The low spread in the total resonance width, illustrated by error bars in Fig. 4, suggests a good quantitative agreement between the measured and calculated RTD conductance. Furthermore, since the only difference between these devices is the setback separating the resonant cavity from the depletion region, these results indicate that the doping spacer helps attenuate the scattering potential associated with ionized donors within the collector region.

To quantify the scattering rate due to ionized impurities in GaN/AlN RTDs, we use the expression:[40]

$$\frac{1}{\tau_{ii}} = \frac{m^\star}{2\pi \hbar^3 k_F^3} \left(\frac{e^2}{2\epsilon_0 \epsilon_s} \right)^2 \int_{x_0}^{x_1} \int_0^{k_F} \frac{N_d(x) e^{-2qx}}{(q + q_{TF})^2} \frac{q^2 dq dx}{\sqrt{1 - \left(\frac{q}{2k_F} \right)^2}},$$
$$(4)$$

where k_F is the Fermi wave-vector. The electric permittivity of free space is ϵ_0, $\epsilon_s = 8.9$ is the relative dielectric constant of GaN, and the Thomas–Fermi wave-number is given by: $q_{TF} = \frac{m^\star e^2}{2\pi \epsilon_0 \epsilon_s \hbar^2}$. $N_d(x)$ is the unscreened donor concentration in the collector depletion region, distributed between the limits: $x_0 = t_b + t_s$ and $x_1 = t_b + t_s + t_d$, as shown in the inset of Fig. 4. t_b is the barrier thickness, t_s is the collector doping setback, and t_d is the extension of the depletion region under forward current injection.

Using Eq. (4), we calculate the partial resonance width due to remote ionized donors given by the relation: $\Gamma_{ii} = \hbar/\tau_{ii}$. To obtain the total width of the resonant level, we also have to include the partial widths Γ_n, arising from other dephasing mechanisms such as background impurities, interface roughness scattering, and electron–electron and electron–phonon interactions. According to the scattering transport theory introduced by Buttiker,[41] we write the total broadening of
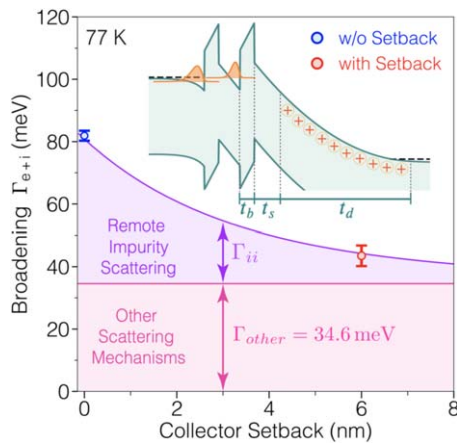
Fig. 4. (Color online) Analysis of the partial contributions to the total width of the resonant level. We experimentally measure the resonance tunneling line width Γ_{e+i} from our fabricated devices [see Fig. 1]. Using an analytical quantum transport model and Eq. (4), we calculate the broadening due to remote impurity scattering, Γ_{ii}, as the collector setback t_s is scaled between 0 and 8 nm. After setting $\Gamma_{other} = 34.6$ meV, we obtain a good quantitative agreement between the measured resonance width and theoretical predictions. Γ_{ii} is calculated under resonant tunneling injection conditions, as shown schematically in the inset. The symbols $\oplus$ indicate the unscreened ionized impurities within the collector depletion region.

the resonant level as the sum of all the partial widths: $\Gamma_{i+e} = \Gamma_{ii} + \Sigma_n \Gamma_n = \Gamma_{ii} + \Gamma_{other}$.

Figure 4 displays the total resonance width (Γ_{e+i}) extracted from our devices, plotted as a function the collector setback t_s. To understand this trend, we calculate Γ_{ii} for the RTD designs shown in Fig. 1, while varying the setback thickness between 0 nm $< t_s <$ 8 nm [see Fig. 4]. As expected, the RTD without doping setback (i.e. $t_s = 0$ nm) exhibits a larger broadening contribution due to stronger coulombic interaction between tunneling electrons and ionized donors within the depletion region. Figure 4 shows that by setting $\Gamma_{other} = 34.6$ meV, we obtain a good quantitative agreement between the theoretical resonance line width and the experimentally measured values from our devices. We highlight that the various scattering rates contained in Γ_{other} are independent of the collector setback, therefore they remain unchanged as t_s is scaled. These results indicate that the introduction of the doping setback helps alleviate, albeit not completely eliminate, decoherence due to ionized impurities. Furthermore, as can be seen from Fig. 4, increasing the collector spacer beyond 6 nm results in an additional reduction in the broadening due to impurity scattering. However, this marginal narrowing in the resonant line width is attained with a concomitant increase in the collector depletion region, thereby exacerbating the asymmetry between the emitter and collector tunneling barriers. In addition, the resonant tunneling voltage also shifts towards higher values, increasing the DC power dissipation at resonance. In this scenario, a detailed RTD transport model that captures these inter-dependencies between structure design and elastic and inelastic scattering rates, would be required to balance the tradeoff between the PVCR and peak current/voltage in a polar GaN/AlN resonant tunneling cavity. The development of this model is beyond the scope of this Letter. However, our analysis reveals the usefulness of our quantum transport model to understand the dephasing processes that limit coherent carrier injection in polar RTDs. This new

insight, reveals a promising route for the improvement of resonant tunneling injection in polar III-nitride RTDs.

To conclude, in this paper, we present a concerted experimental and theoretical study that clarifies the impact of the collector doping setback on the broadening of the resonant tunneling line shape. These effects are experimentally investigated by measuring the electronic transport characteristics of GaN/AlN RTDs with different collector doping setbacks. Employing our analytical model for resonant tunneling transport, we quantify the broadening of the resonance line shape, conclusively demonstrating that the inclusion of the doping setback helps preserve coherent tunneling injection. This design allows us to measure consistently higher PVCRs, obtaining a maximum PVCR of 2.01 at cryogenic temperatures.

ORCID iDs Jimy Encomendero https://orcid.org/0000-0002-1597-1761

1) J. Federici and L. Moeller, J. Appl. Phys. **107**, 111101 (2010).
2) N. Oshima, K. Hashimoto, S. Suzuki, and M. Asada, IEEE Trans. Terahertz Sci. Technol. **7**, 593 (2017).
3) T. Maekawa, H. Kanaya, S. Suzuki, and M. Asada, Appl. Phys. Express **9**, 024101 (2016).
4) Y. Koyama, R. Sekiguchi, and T. Ouchi, Appl. Phys. Express **6**, 064102 (2013).
5) T. Miyamoto, A. Yamaguchi, and T. Mukai, Jpn. J. Appl. Phys. **55**, 032201 (2016).
6) S. Kitagawa, M. Mizuno, S. Saito, K. Ogino, S. Suzuki, and M. Asada, Jpn. J. Appl. Phys. **56**, 058002 (2017).
7) C. Sirtori, F. Capasso, J. Faist, A. L. Hutchinson, D. L. Sivco, and A. Y. Cho, IEEE J. Quantum Electron. **34**, 1722 (1998).
8) H. Kanaya, T. Maekawa, S. Suzuki, and M. Asada, Jpn. J. Appl. Phys. **54**, 094103 (2015).
9) M. Egard, M. Arlelid, L. Ohlsson, B. M. Borg, E. Lind, and L.-e. Wernersson, IEEE Electron Device Lett. **33**, 970 (2012).
10) S. Kitagawa, S. Suzuki, and M. Asada, IEEE Electron Device Lett. **35**, 1215–7 (2014).
11) R. Izumi, S. Suzuki, and M. Asada, 42nd Int. Conf. on Infrared, Millimeter, and Terahertz Waves (IRMMW-THz), 2017, p. 1.
12) J. Faist, F. Capasso, D. L. Sivco, C. Sirtori, A. L. Hutchinson, and A. Y. Cho, Science **264**, 553 (1994).
13) S. Sakr, Y. Kotsar, M. Tchernycheva, E. Warde, N. Isac, E. Monroy, and F. H. Julien, Appl. Phys. Express **5**, 052203 (2012).
14) J. Encomendero, F. Afzo Faria, S. M. Islam, V. Protasenko, S. Rouvimov, P. Fay, D. Jena, and H. G. Xing, arXiv:1606.08100 (2016).
15) T. A. Growden, D. F. Storm, W. Zhang, E. R. Brown, D. J. Meyer, P. Fakhimi, and P. R. Berger, Appl. Phys. Lett. **109**, 083504 (2016).
16) T. A. Growden et al., Appl. Phys. Lett. **116**, 113501 (2020).
17) D. Wang et al., Adv. Electron. Mater. **1800651**, 1800651 (2018).
18) D. Wang et al., Appl. Phys. Lett. **114**, 073503 (2019).
19) J. Encomendero, F. A. Faria, S. M. Islam, V. Protasenko, S. Rouvimov, B. Sensale-Rodriguez, P. Fay, D. Jena, and H. G. Xing, Phys. Rev. X **7**, 041017 (2017).
20) J. Encomendero, V. Protasenko, F. Rana, D. Jena, and H. G. Xing, Phys. Rev. Appl. **13**, 034048 (2020).
21) H. G. Xing, J. Encomendero, and D. Jena, Proc. SPIE **10918**, 109180Z (2019).
22) J. Encomendero, S. Islam, D. Jena, and H. Grace Xing, J. Vac. Sci. Technol. A **39**, 023409 (2021).
23) T. A. Growden, W. Zhang, E. R. Brown, D. F. Storm, K. Hansen, P. Fakhimi, D. J. Meyer, and P. R. Berger, Appl. Phys. Lett. **112**, 033508 (2018).
24) J. Encomendero, R. Yan, A. Verma, S. M. Islam, V. Protasenko, S. Rouvimov, P. Fay, D. Jena, and H. G. Xing, Appl. Phys. Lett. **112**, 103101 (2018).

25) Y. Cho, J. Encomendero, S.-T. Ho, H. G. Xing, and D. Jena, Appl. Phys. Lett. **117**, 143501 (2020).
26) H. G. Xing, R. Yan, B. Song, J. Encomendero, and D. Jena, Proc. SPIE **9476**, 94760Q (2016).
27) H. O. Condori Quispe, J. J. Encomendero-Risco, H. G. Xing, and B. Sensale-Rodriguez, Appl. Phys. Lett. **109**, 063111 (2016).
28) H. O. C. Quispe, J. Encomendero, H. G. Xing, and B. S. Rodriguez, Proc. SPIE **9920**, 992027 (2015).
29) H. O. Condori Quispe, A. Chanana, J. Encomendero, M. Zhu, N. Trometer, A. Nahata, D. Jena, H. G. Xing, and B. Sensale-Rodriguez, J. Appl. Phys. **124**, 093101 (2018).
30) J. Encomendero, D. Jena, and H. G. Xing, *Resonant Tunneling Transport in Polar III-Nitride Heterostructures, in High-Frequency GaN Electronic Devices* (Springer, Cham, 2020) , p. 215.
31) M. A. Moram and M. E. Vickers, Rep. Prog. Phys. **72**, 036502 (2009).
32) C. I. Huang, M. J. Paulus, C. A. Bozada, S. C. Dudley, K. R. Evans, C. E. Stutz, R. L. Jones, and M. E. Cheney, Appl. Phys. Lett. **51**, 121 (1987).
33) I. Mehdi, R. K. Mains, and G. I. Haddad, Appl. Phys. Lett. **57**, 899 (1990).
34) S. Muto, T. Inata, H. Ohnishi, N. Yokoyama, and S. Hiyamizu, Jpn. J. Appl. Phys. **25**, L577 (1986).
35) T. Oobo, R. Takemura, K. Sato, M. Suhara, Y. Miyamoto, and K. Furuya, Jpn. J. Appl. Phys. **37**, 445 (1998).
36) J. Encomendero, V. Protasenko, B. Sensale-Rodriguez, P. Fay, F. Rana, D. Jena, and H. G. Xing, Phys. Rev. Appl. **11**, 034032 (2019).
37) J. Chen, J. G. Chen, C. H. Yang, and R. A. Wilson, J. Appl. Phys. **70**, 3131 (1991).
38) P. J. Price, Phys. Rev. B **45**, 9042 (1992).
39) H. Sheng and J. Sinkkonen, Superlattices Microstruct. **12**, 453–7 (1992).
40) J. Davies and J. Davies, *The Physics of Low-dimensional Semiconductors: An Introduction* (Cambridge University Press, Cambridge, 1998).
41) M. Buttiker, IBM J. Res. Dev. **32**, 63 (1988).